Metabolic Engineering 67 (2021) 41–52

Contents lists available at ScienceDirect

Metabolic Engineering

journal homepage: www.elsevier.com/locate/meteng

Development of a growth coupled and multi-layered dynamic regulation network balancing malonyl-CoA node to enhance (2*S*)-naringenin biosynthesis in *Escherichia coli*☆

Shenghu Zhou [a,b,1], Shuo-Fu Yuan [c,1], Priya H. Nair [d], Hal S. Alper [c,d], Yu Deng [a,b,*], Jingwen Zhou [a,b,e,**]

[a] National Engineering Laboratory for Cereal Fermentation Technology (NELCF), Jiangnan University, 1800 Lihu Road, Wuxi, Jiangsu, 214122, China
[b] Science Center for Future Foods, Jiangnan University, 1800 Lihu Road, Wuxi, Jiangsu, 214122, China
[c] Institute for Cellular and Molecular Biology, The University of Texas at Austin, 2500 Speedway Avenue, Austin, TX, 78712, USA
[d] McKetta Department of Chemical Engineering, The University of Texas at Austin, 200 E Dean Keeton St. Stop C0400, Austin, TX, 78712, USA
[e] Jiangsu Provincial Research Center for Bioactive Product Processing Technology, Jiangnan University, 1800 Lihu Road, Wuxi, Jiangsu, 214122, China

ARTICLE INFO

Keywords:
Acyl carrier protein
p-Coumaric acid
Directed evolution
Dynamic regulation network
Malonyl-CoA
(2*S*)-Naringenin

ABSTRACT

Metabolic heterogeneity and dynamic changes in metabolic fluxes are two inherent characteristics of microbial fermentation that limit the precise control of metabolisms, often leading to impaired cell growth and low productivity. Dynamic metabolic engineering addresses these challenges through the design of multi-layered and multi-genetic dynamic regulation network (DRN) that allow a single cell to autonomously adjust metabolic flux in response to its growth and metabolite accumulation conditions. Here, we developed a growth coupled NCOMB (Naringenin-Coumaric acid-Malonyl-CoA-Balanced) DRN with systematic optimization of (2*S*)-naringenin and *p*-coumaric acid-responsive regulation pathways for real-time control of intracellular supply of malonyl-CoA. In this scenario, the acyl carrier protein was used as a novel critical node for fine-tuning malonyl-CoA consumption instead of direct repression of fatty acid synthase commonly employed in previous studies. To do so, we first engineered a multi-layered DRN enabling single cells to concurrently regulate *acpH*, *acpS*, *acpT*, *acs*, and *ACC* in malonyl-CoA catabolic and anabolic pathways. Next, the NCOMB DRN was optimized to enhance the synergies between different dynamic regulation layers via a biosensor-based directed evolution strategy. Finally, a high producer obtained from NCOMB DRN approach yielded a 8.7-fold improvement in (2*S*)-naringenin production (523.7 ± 51.8 mg/L) with a concomitant 20% increase in cell growth compared to the base strain using static strain engineering approach, thus demonstrating the high efficiency of this system for improving pathway production.

1. Introduction

Microbial production of value-added biochemicals often requires the development of a robust, efficient, and high-performance strain. To this end, static metabolic engineering strategies including multi-module optimization (Wu et al., 2013), promoter and RBS engineering (Zhang et al., 2015), and CRISPR/Cas9-based genome engineering (Ran et al., 2013) are commonly employed for rewiring metabolic flux to maximize production. Despite significant successes in the literature and industry using these static strain engineering paradigms, it remains difficult to balance the trade-offs between growth and production. To address this imbalance within static strain engineering approaches, researchers often

☆ Mailing address: National Engineering Laboratory for Cereal Fermentation Technology, 1800 Lihu Road, Wuxi, Jiangsu 214122, China. Phone: +86-85914371, Fax: +86-510-85914371.
* Corresponding author. National Engineering Laboratory for Cereal Fermentation Technology (NELCF), Jiangnan University, 1800 Lihu Road, Wuxi, Jiangsu, 214122, China.
** Corresponding author. National Engineering Laboratory for Cereal Fermentation Technology (NELCF), Jiangnan University, 1800 Lihu Road, Wuxi, Jiangsu, 214122, China.
E-mail addresses: dengyu@jiangnan.edu.cn (Y. Deng), zhoujw1982@jiangnan.edu.cn (J. Zhou).
[1] Shenghu Zhou and Shuo-Fu Yuan contributed equally.

https://doi.org/10.1016/j.ymben.2021.05.007
Received 14 January 2021; Received in revised form 29 April 2021; Accepted 21 May 2021
Available online 27 May 2021
1096-7176/© 2021 International Metabolic Engineering Society. Published by Elsevier Inc. All rights reserved.

control the changes in fermentation conditions including dynamic control of environmental changes such as incubation temperature, osmolarity, and inducer and nutrient availability (Schmidt, 2005; Singh et al., 2017). As an alternative, genetic approach with the use of transcription factor-based biosensors provides the potential for enabling real-time monitoring of cell growth and/or metabolite production and dynamically regulating pathway-relevant gene expression in response to intracellular signals (Moser et al., 2018).

Using the principles of dynamic regulation, a series of control systems (typically enabled by biosensors) fine-tune the cells to synthesize a target compound at maximum production levels (Shen et al., 2019). These control systems can be dynamically regulated at either the environmental or metabolic level. Generally, biosensors that could respond to universal, environmental induction factors such as temperature (Zheng et al., 2019), dissolved oxygen (Moser et al., 2018), cell density (Tian et al., 2020), and light (Zhao et al., 2019) enable construction of environment-responding dynamic regulation networks (DRNs). While these biosensors can dynamically modulate gene expression of all cells in response to the global environment changes, namely "population regulation", the differences between intracellular states of single cells are often overlooked. More specifically, fermentation conditions such as cell density represent the overall state of the cell population. In reality, a culture contains a mixture of both young and aged cells with concomitant high- and low-performance cells in all growth phases, which is so called metabolic heterogeneity (Xiao et al., 2016). As a result, precisely regulating metabolic flux based on the intracellular state can help improve overall productivity within a fermentation. To this end, it is important to identify biosensors that can directly monitor the intracellular metabolic state of single cells and thus individually regulate gene expression within single cells in response to a critical metabolite level (Shen et al., 2019).

Generally, spatial distribution states of inducers directly influence the biosensor responsive mode. Environmental induction and extracellular metabolites responsive biosensors could confer a "population regulation" phenomenon which regulates and synchronizes cellular gene expression at a singular, special induction point without considering differences between single-cell states under different conditions. In contrast, intracellular metabolites responsive biosensors could fine-tune the target gene expression of individual cells by reflecting on the specific, single-cell metabolite accumulation levels, thus leading to a more optimized ensemble of cells. Recent examples that aim to dynamically regulate the metabolic flux of single cells have been used to balance malonyl-CoA as it only exists intracellularly. For example, by coupling the glucose-responsive promoter (P_{HXT1}) with a malonyl-CoA sensitive transcriptional repressor (FapR), David et al. constructed a DRN to drive the flux from the malonyl-CoA pool toward 3-hydroxypropionic acid formation, leading to a 10-fold increase in titer (David et al., 2016). Additionally, Xu et al. developed an oscillator to dynamically balance malonyl-CoA pool through controlling the expression of acetyl-CoA carboxylase (ACC) and fatty acid synthase (Xu et al., 2014). In their report, the best producer displayed a 2.1-fold improvement in fatty acids titer (3.86 g/L). While successful in improving product titers, metabolite-responsive DRNs only monitor the fluctuating level of a metabolite without coupling with the growth profile of single cells, usually at the expense of growth.

Currently, quorum sensing (QS)-based dynamic regulation is the most popular strategy for coupling cellular growth and metabolites production (Ge et al., 2020; Tian et al., 2020). However, the transmembrane transport of QS signal molecules N-acyl homoserine lactones (AHLs) is freely diffusible and accompanied by active efflux, leading to the same intra- and extracellular concentrations (Minagawa et al., 2012; Pearson et al., 1999). Hence, QS-based dynamic regulation is a typical "population regulation" strategy that overlooked the differences between single cells. Moreover, simply synchronizing cells based on growth state overlooks the differences in intracellular metabolite fluxes across individual cells. To date, growth coupled single-cell level dynamic regulation is still rarely explored. In particular, such a design often requires the dynamic control of several critical metabolic nodes simultaneously to control metabolic flux distribution. By taking cell growth, product synthesis, and transient changes in intermediate metabolite accumulation states into account, these more complex dynamic control systems multi-layered and sophisticated DRNs. However, it is difficult to modulate the regulation manner (up-regulation or down-regulation) and expression level of various genes between different DRN layers.

To address this challenge, the work present here demonstrates an optimized layered dynamic regulation device that implements a growth coupled single cell sensing and regulating DRNs cascade to improve the production of the flavonoid (2*S*)-naringenin. Specifically, this DRN cascade focuses on dynamically regulating the expression of 5 genes (*acpH*, *acpS*, *acpT*, *acs*, and *ACC*) closely related to supply of malonyl-CoA, a crucial metabolite used as a carbon-chain elongation unit for important compounds such as flavonoids (Palmer et al., 2020; Zhou et al., 2019, 2020abib_Zhou_et_al_2020abib_Zhou_et_al_2019), antibiotics (Bretschneider et al., 2011), and fatty acids (Milke and Marienhagen; Xu et al., 2014). Generally, the availability of intracellular malonyl-CoA is limited and reduces from 0.23 to 0.01 nmol/(mg dry wt) when cells transit from exponential to stationary stage (Takamura and Nomura, 1988). Traditional approaches to increase malonyl-CoA content usually represses the fatty acid biosynthetic pathway (Yang et al., 2015). However, excessive repression of this pathway leads to impaired cell growth. Additionally, oversupply of malonyl-CoA causes an undesired malonylation of the proteome, thus establishing a further carbon burden in engineered *E. coli* (Xu et al., 2018). As a result, malonyl-CoA must be in an exquisite balance within cells. In this study, we designed and optimized a metabolite-responsive NCOMB (Naringenin-Coumaric acid-Malonyl-CoA-Balanced) DRN which can real-time monitor the intracellular concentration of (2*S*)-naringenin and *p*-coumaric acid to dynamically enhance the production of malonyl-CoA at all growth phases. The designed DRN includes three layers: Layer I that functionally produces (2*S*)-naringenin; Layer II that dynamically amplifies the metabolic flux toward the (2*S*)-naringenin synthetic pathway by coupling cell growth; Layer III that dynamically responds to *p*-coumaric acid and enhances the production of malonyl-CoA during late stages of fermentation (Fig. 1). In doing so, we successfully demonstrate the ability of NCOMB DRN to achieve single cell dynamic regulation and a balance of (2*S*)-naringenin production with cell growth based on the level of intracellular metabolite, which could further facilitate the application of DRN in the complicated metabolic network.

2. Results

2.1. Comparison of intra- and extra-cellular concentrations of (2S)-naringenin and p-coumaric acid

To evaluate the efficacy of a biosensor-based control approach, we measured the spatiotemporal distribution of (2*S*)-naringenin and *p*-coumaric acid. In doing so, we measured the intracellular and extracellular content of (2*S*)-naringenin and *p*-coumaric acid using the previously constructed (2*S*)-naringenin producer (9G3) (Zhou et al., 2019). The results indicated that the intracellular concentration of (2*S*)-naringenin and *p*-coumaric acid is much higher than extracellular content in both the log phase and stationary phase (Fig. 2). Specifically, the intracellular level of (2*S*)-naringenin and *p*-coumaric acid is at least 58.1- and 10.2-fold higher than the extracellular content across all growth phases, respectively. These results indicate that the transport efficiency of (2*S*)-naringenin and *p*-coumaric acid out of the cell was limited, making each cell relatively independent with a minimal cross-talk. As a result, we posit that the intracellular accumulation states of (2*S*)-naringenin and *p*-coumaric acid will reflect the metabolic states of individual cells. Hence, utilization of intracellular (2*S*)-naringenin and *p*-coumaric acid biosensors can achieve single cell dynamic regulation as

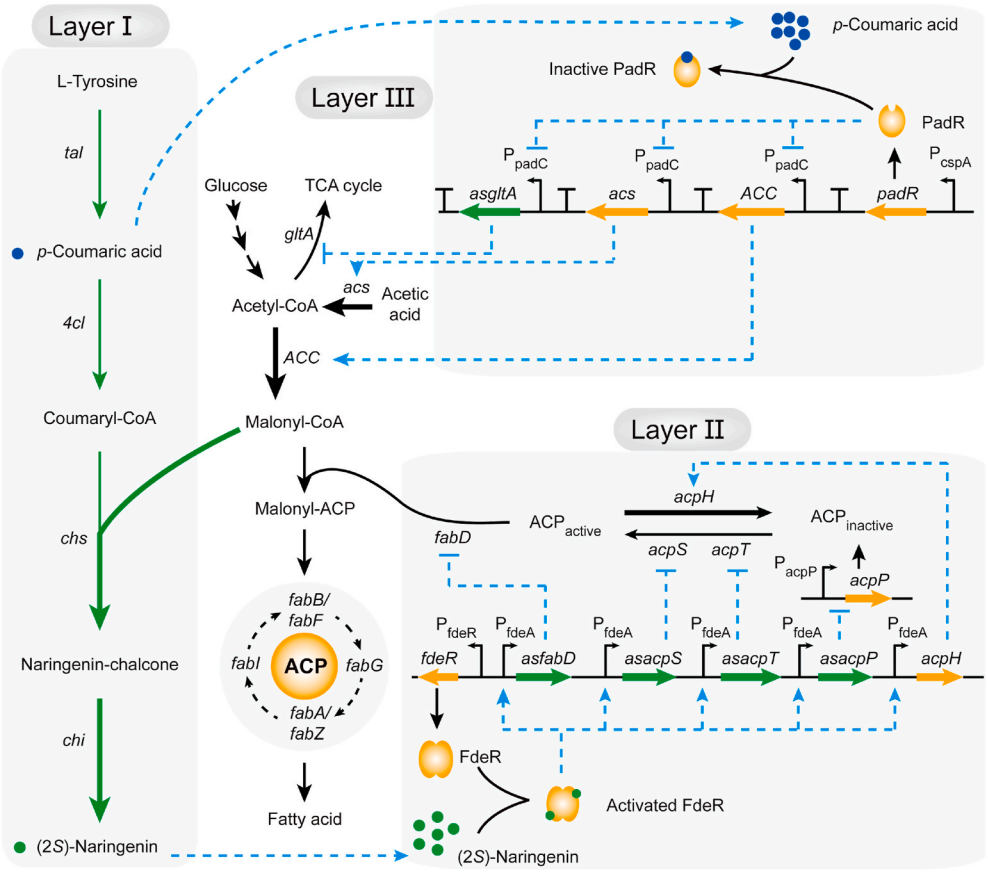

Fig. 1. Schematic of the mechanisms for the NCOMB DRN.
Layer I: Heterologous (2*S*)-naringenin biosynthesis pathway; Layer II: Fatty acid repression module. Layer I and II could constitute to be a (2*S*)-naringenin-responsive amplification system to gradually elevate the repression level in malonyl-CoA consumption pathway over the course of the fermentation; Layer III: Malonyl-CoA enhancing module. *p*-Coumaric acid-responsive pathway can dynamically enhance the supply of malonyl-CoA at stationary growth phase. Gene and protein annotations: tyrosine ammonia-lyase (*tal*), 4-coumarate: CoA ligase (4 cl), chalcone synthase (*chs*), chalcone isomerase (*chi*), citrate synthase (*gltA*), acetyl-CoA synthetase (*acs*), acetyl-CoA carboxylase (ACC), acyl carrier protein (ACP), flavonoids-responsive transcriptional activator from *Herbaspirillum seropedicae* SmR1 (FdeR), *p*-coumaric acid-responsive transcriptional repressor from *Bacillus subtilis* (PadR), acyl carrier protein phosphodiesterase (*acpH*). *asfabD*, *asacpS*, *asacpT*, *asacpP*, and *asgltA* are anti-sense RNAs. Green arrows: constitutive expression pathway. Blue dash arrows: activation reactions; Blue dash blunt arrows: repression reactions. Bold arrows: enhanced metabolic fluxes.

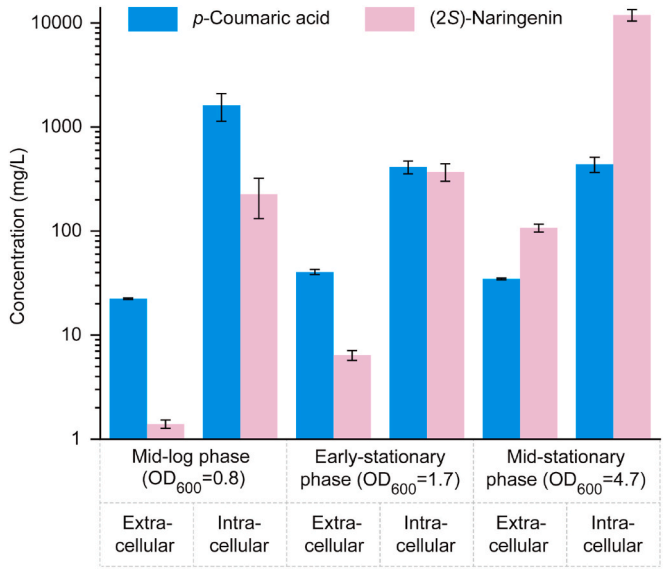

Fig. 2. Intra- and extra-cellular accumulation states of (2*S*)-naringenin- and *p*-coumaric acid in different growth phases.
Strain 9G3 is a strain that not only carries Layer I, but also simultaneously constitutively expressed malonate synthetase (*matB*) and malonate carrier protein (*matC*). *matBC* could convert the added malonic acid to malonyl-CoA for the biosynthesis of (2*S*)-naringenin. Error bars represent standard deviation of biological triplicate experiments. The detailed calculation method of intra- and extra-cellular contents were described in Materials and methods 4.7.

a means to maximize (2*S*)-naringenin production.

2.2. Construction and optimization of critical DRN biosensors

The (2*S*)-naringenin (FdeR based)- (Siedler et al., 2014; Wassem et al., 2017) and *p*-coumaric acid (PadR based)- (Siedler et al., 2017) responsive biosensors are the central regulatory elements of our NCOMB DRN. To fine-tune the transcription of downstream target genes, it was necessary to engineer a tight control of these elements. Although the responsive promoter architecture of P_{fdeA} (Wassem et al., 2017) and P_{padC} (Nguyen et al., 2011; Tran et al., 2008) have been reported, information of the coresponding promoter strength is still unclear. Given that the excess length of 5′-UTR region for the P_{fdeA} and P_{padC} could change the secondary structure of anti-sense RNA and affect the expression of target genes in our DRN design (Fig. 1), we first generated a series of truncated promoters to thoroughly investigate their impacts on the expression of corresponding genes of interest.

P_{fdeA} is a bidirectional promoter 288 bp in length and contains a dozen FdeR binding sites (T-N11-A) spread over a wide region (Wassem et al., 2017). To dissect function of this element, we truncated P_{fdeA} in both directions based on the position of FdeR binding sites and generated 8 variants of P_{fdeA} (M-N) promoter actuated biosensors (Fig. 3a and Supplementary Fig. 1a). As a result, we identified that the shorter version of P_{fdeA}(223-135), only 88 bp in length, exhibited around 4-fold higher signal-to-noise ratio than that of the orginal P_{fdeA} (288-1) when induced by 50 mg/L of (2*S*)-naringenin (Fig. 3b and c). Furthermore, the sensor with the truncated promoter P_{fdeA} (223-135) displayed a highest sensitivity over other constructs (Supplementary Fig. 1b). These properities can enable the newly designed (2*S*)-naringenin-responsive biosensor to express anti-sense RNAs and proteins (Fig. 1) at a very low level of (2*S*)-naringenin.

Turning to the second P_{padC} promoter system, used to control the

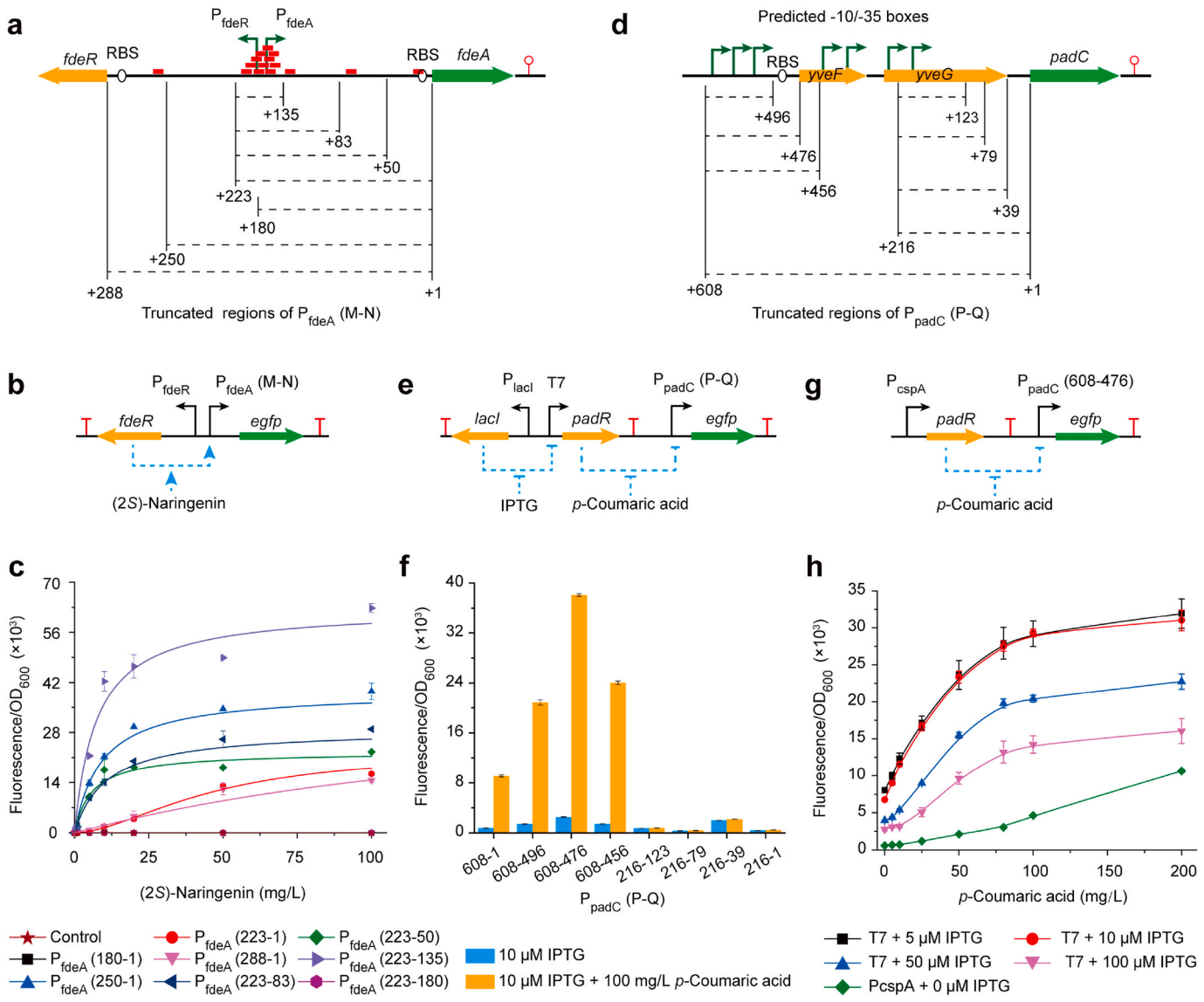

Fig. 3. The structures and properties of (2*S*)-naringenin- and *p*-coumaric acid-responsive biosensors. a: The original structure of P_{fdeA} bidirectional promoter and truncated P_{fdeA} (M–N) regions. Red bar represents FdeR binding site (T-N11-A). b: The structure of (2*S*)-naringenin-responsive biosensor. c: The expression strength of promoter P_{fdeA} (M–N) when induced by various concentrations of (2*S*)-naringenin. Control represents strain only harboring pRSM-FdeR. Strains labeled with M-N represent constructs carrying pCDM-PfdeA(M-N)-GFP and pRSM-FdeR (Supplementary Fig. 1a). d: The predicted −35/-10 boxes of P_{padC} and truncated P_{padC}(P-Q) regions. e: The structure of IPTG- and *p*-coumaric acid responsive biosensor. f: The expression strength of promoter P_{padC} (P–Q). g: The structure of *p*-coumaric acid-responsive biosensor. h: Comparison of the properties of IPTG and/or *p*-coumaric acid inducible biosensors. Blue dash arrows: activation reactions; Blue dash blunt arrows: repression reactions. Means are reported, and the error bars represent standard deviation of biological triplicates.

expression of *yveF*, *yveG*, and *padC* in an operon form, we predicted that the position of potential −35/-10 boxes by BDGP neural network promoter prediction software v2.2 (Reese, 2001) and idenfied 7 candidate sites (Fig. 3d). In a similar fashion with P_{fdeA}, we established a promoter truncation series for P_{padC} based on the position of predicted −35/-10 boxes. Using the truncated promoter P_{padC}(P-Q), 8 variants of *p*-coumaric acid and IPTG-responsive biosensors were constructed and evaluated (Fig. 3e and Supplementary Fig. 1c). As shown in Fig. 3f, the position of 608-476 was identified as a suitable region for protein expression, which demonstrated a 4.2-fold higher expression than that of the original P_{padC} (608-1). Furthermore, the shortest version (608-496) without the RBS exhibited an ideal expression strength, 2.3-fold of that of the original P_{padC} (608-1), which could be also used for expression of anti-sense RNA. To avoid the use of inherently leaky expression and expensive inducer in T7-based inducible system, we next employed a exponential phase-induced promoter P_{cspA} (Zhou et al., 2017) to control the expression of PadR (Fig. 3g). Compared with the T7 promoter, P_{cspA} exbibited lower leaky expression with only 7.2% of that when 5 μM IPTG was added to the medium (Fig. 3h). Despite the lower total responsive level of P_{cspA} (only 33.3% of 5 μM IPTG-induced T7 controlled biosensor (Fig. 3h)), the dynamic range of *p*-coumaric acid response was 18.2-fold higher in this system compared with the T7 controlled biosensor system. Previous study has demonstrated that the expression level of P_{cspA} in exponential phase was 11.9-fold higher than in stationary phase (Zhou et al., 2017), implying tightly controlling target gene expression in stationary phase could be achieved with the use of P_{cspA} system.

2.3. Optimization of the fatty acid synthetic pathway

Most cellular malonyl-CoA in wild-type cells is consumed by the fatty acid synthetic pathway which requires an acyl carrier protein (ACP) to

convert malonyl-CoA to fatty acyl-ACP for extending the saturated fatty acyl chain in each elongation cycle (Chan and Vogel, 2010). Considering the important role of cofactor protein ACP in the fatty acid synthetic pathway, the consumption of malonyl-CoA could be regulated by fine-tuning the activity of ACP. To do so, we overexpressed acyl carrier protein phosphodiesterase (*acpH*) to accelerate the transition from ACP_{active} to $ACP_{inactive}$ (Thomas and Cronan, 2005). Furthermore, the anti-sense RNA of *acpS*, *acpT*, *acpP*, and *fabD* were also overexpressed to repress the translation of ACP, the transition from $ACP_{inactive}$ to ACP_{active}, and the formation of malonyl-ACP (Fig. 1). Through the combinatorial regulation of these genes, the concentration of malonyl-CoA was improved to at least 3.61-fold of that of control (Fig. 4). Through this analysis, we observed that accumulation of intracellular malonyl-CoA led to a lower biomass formation (Fig. 4), suggesting a proper dynamic control of expression level of *acpH* as*acpS*, and as*acpT* is necessary to balance between cell growth and malonyl-CoA accumulation.

Taken together, these results demonstrate that the repression of the transition form $ACP_{inactive}$ to ACP_{active} state is more efficient than repressing ACP translation and malonyl-ACP formation (Figs. 1 and 4). This could be explained by the rapid turnover of the AcpS and AcpT catalyzed reaction, thus resulting in almost exclusive ACP_{active} form (Heil et al., 2019). Furthermore, overexpression of AcpH not only suppresses the activity of ACP, but could also hydrolyze the 4′-phosphopantetheine moiety of ACP resulting in increasing amounts of CoA and acetyl-CoA after ACP repression (Supplementary Fig. 2) (Sibon and Strauss, 2016). Subsequently, the increased CoA and acetyl-CoA further enhance the biosynthesis of malonyl-CoA. Comparing with the commonly used strategy to repress target fatty acid synthase (Yang et al., 2015), the repression of ACP is a feasible route to promote the recycling of CoA.

2.4. Designing a (2*S*)-naringenin-responsive amplifier to balance growth and malonyl-CoA accumulation

In order to dynamically control cell growth and intracellular malonyl-CoA availability, we attempted to construct a (2*S*)-naringenin-responsive amplifier through coupling the previously optimized (2*S*)-naringenin synthetic pathway (Layer I) (Zhou et al., 2019) with the abovementioned fatty acid repression module (Layer II) (Fig. 5a). This amplifier could dynamically repress the ACP activity for malonyl-CoA allocation between cell growth and (2*S*)-naringenin biosynthesis based on the cellular (2*S*)-naringenin content. At the early growth stage, the fast cellular division requires a large amount of malonyl-CoA for cell membrane formation. However, in the middle and later growth stage, fewer malonyl-CoA is needed for cell membrane biosynthesis. In this background, a low level of (2*S*)-naringenin that synthesized by the constitutively expressed Layer I at early growth stage will weakly activate Layer II, thus slowly repress the activity of ACP to produce just enough fatty acid to support cell membrane formation. As the cell growth, the amount of (2*S*)-naringenin progressively increased, which will gradually enhance the repression of ACP expression, thus further improving malonyl-CoA supply and (2*S*)-naringenin production. In this scenario, the amplifier could dynamically incrementally redirect the malonyl-CoA from fatty acid synthesis to (2*S*)-naringenin synthetic pathway without negative impact on cell growth (Fig. 5a).

To verify this concept, (2*S*)-naringenin titer and the expression level of *acpH*, as*acpS*, and as*acpT* was determined over the course of fermentation for the engineered strain harboring (2*S*)-naringenin-responsive amplifier. Specifically, we observed a strong positive correlation between fermentation time, (2*S*)-naringenin content and the transcription level of *acpH*, as*acpS*, and as*acpT* (Fig. 5b). The highest normalized expression levels of *acpH*, as*acpS*, and as*acpT* were 3945, 803, and 4983, respectively, when (2*S*)-naringenin titer reached 79.2 mg/L (Fig. 5b). These results indicate that the constructed amplifier can respond to a broad range of (2*S*)-naringenin concentrations.

To further optimize cell growth, we utilized a three-plasmid system with varying copy numbers to modulate expression levels of Layer II for properly regulating fatty acid biosynthesis and cell growth. In doing so, the (2*S*)-naringenin titer was improved 2.2- to 3.2-fold compared with the control strain only expressing Layer I (Nar_{modA}) without any impact on cell growth (Fig. 5c–f). As a result, the low copy number of Layer II was selected as the optimal module for (2*S*)-naringenin production. Comparing with the Nar_{modA}, the accumulation of intermediate *p*-coumaric acid significantly decreased in Layer II-combined strains after 14 h fermentation (Fig. 5c–f). This phenomenon could attribute to Layer II function which improved the supply of malonyl-CoA and thus increased the metabolic flux from *p*-coumaric acid to (2*S*)-naringenin biosynthesis. However, the *p*-coumaric acid in Layer II-combined strains rapidly accumulated and (2*S*)-naringenin production reached a plateau after cell growth entered a stationary phase (Fig. 5d–f). Therefore, the critical challenge left to further improve (2*S*)-naringenin production would be to efficiently utilize the build-up of *p*-coumaric acid in stationary phase.

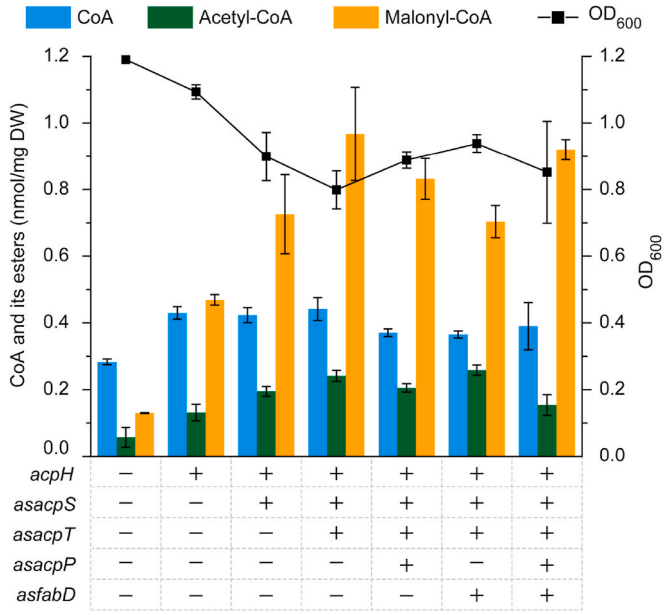

Fig. 4. Fatty acid pathway optimization by (2*S*)-naringenin-responsive biosensor.
Genes were overexpressed in pACM-FdeR plasmid under the control of P_{fdeA} (223-135) with 100 mg/L (2*S*)-naringenin induction. + or - represent the related genes were overexpressed or not, respectively. The control strain only harboring pACM-FdeR. Means are reported, and the error bars represent standard deviation of biological triplicates.

2.5. Malonyl-CoA synthetic pathway optimization via *p*-coumaric acid-responsive biosensor

Previous study has demonstrated that the concentrations of acetyl-CoA and malonyl-CoA reached the highest levels in exponential phase and rapidly fell to 6.7% and 12.5% of the maximum level when entering stationary phase, respectively (Takamura and Nomura, 1988). Hence, we hypothesize that the accumulation of *p*-coumaric acid and decrease in (2*S*)-naringenin productivity observed in stationary phase was due to the limited availability of malonyl-CoA resulted from the reduced metabolic flux to biosynthesis of acetyl-CoA and malonyl-CoA in the stationary phase. To verify this hypothesis, we measured the concentration of malonyl-CoA in wild type *E. coli* BL21 at different growth phases and confirmed that malonyl-CoA reached its highest level in early growth stage and was almost undetectable in stationary phase (Fig. 6a). To enhance the intracellular level of malonyl-CoA, we constructed a dynamically regulated strain, Nar_{modAC} (Fig. 6b), through combining the *p*-coumaric acid-responsive dynamic regulation module

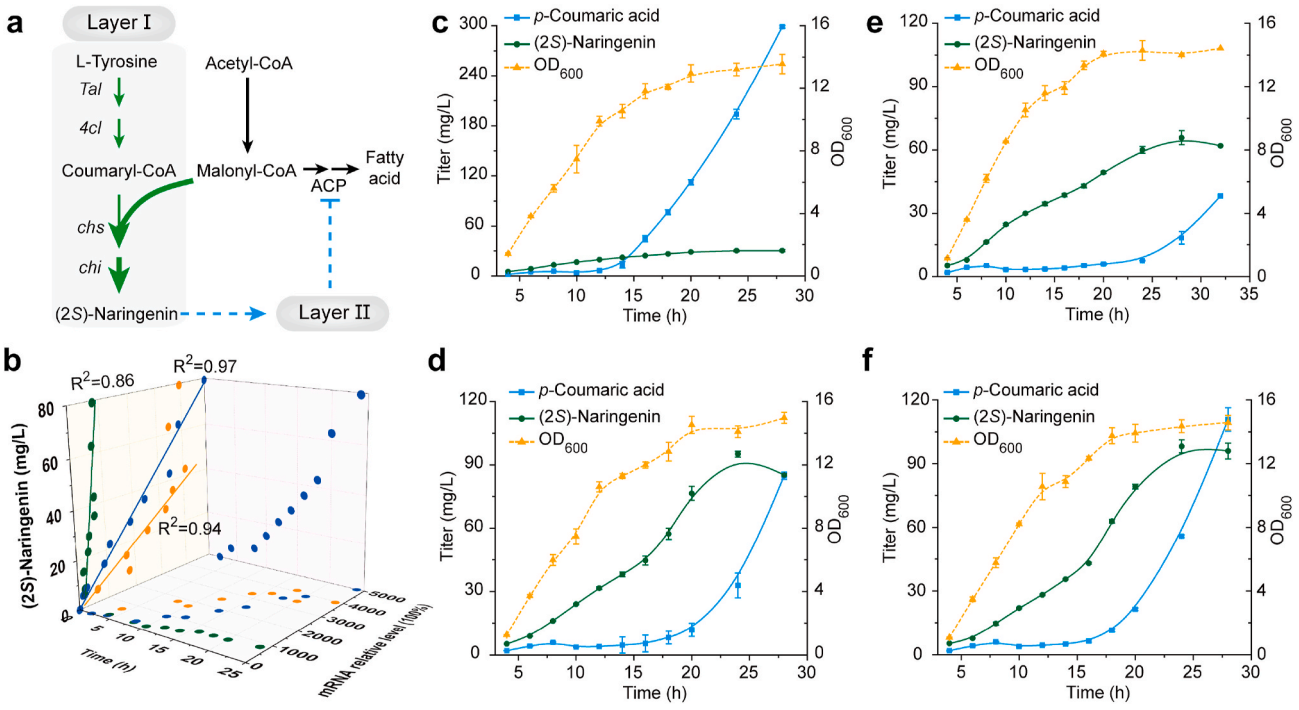

Fig. 5. The mechanisms and properties of (2*S*)-naringenin-responsive amplifier. **a**: The mechanisms of (2*S*)-naringenin-responsive amplifier. Green arrows: constitutive expression pathway. Blue dash arrows: activation reactions; Blue dash blunt arrows: repression reactions. **b**: The relative mRNA level and (2*S*)-naringenin titer of Layer I and II combined strain at different fermentation time. pACM-FdeR-*acpH*-as*acpT*-as*acpS* was used as Layer II. Blue, green, and orange points represent as*acpT*, as*acpS*, and *acpH* genes, respectively. In the Time *v.s.* (2*S*)-naringenin coordinate, the data points for all 3 genes were the same, hence only the blue points were shown. **c-f**: The fermentation of different Layer I and II combined strains. The control strain (Nar_{modA}) only harbors Layer I (**c**). Layer I combined with pACM-FdeR-*acpH*-as*acpT*-as*acpS* (low copy number), pCOM-FdeR-*acpH*-as*acpT*-as*acpS* (medium copy number), pRSM-FdeR-*acpH*-as*acpT*-as*acpS* (high copy number) to generate strains of $Nar_{modAB\text{-}L}$ (**d**), $Nar_{modAB\text{-}M}$ (**e**), and $Nar_{modAB\text{-}H}$ (**f**), respectively. Means are reported, and the error bars represent standard deviation of biological triplicates.

(Layer III in Fig. 1) with Layer I. In doing so, the biosynthesis of malonyl-CoA would be enhanced via overexpression of *acs*, *ACC*, and the anti-sense RNA of *gltA* (as*gltA*) when *p*-coumaric acid accumulated. In order to optimize this Layer III, the combinatorial overexpression of *acs*, *ACC*, and as*gltA* was evaluated and we found that overexpression of these genes facilitated the biosynthesis of (2*S*)-naringenin. Among all the constructs, simultaneous overexpression of *acs* and *ACC* leads to the highest (2*S*)-naringenin titer which was 1.5-fold higher than that of Nar_{modA} (Fig. 6c).

2.6. Complete DRN assembly for (2S)-naringenin production

Based on these collective results and all modules in place, we combined the optimized layers I, II, and III to construct an artificial DRN which could simultaneously respond with (2*S*)-naringenin and *p*-coumaric acid to dynamically regulate the metabolic flux of consumption and biosynthesis of malonyl-CoA, respectively (Figs. 1 and 6d). Our system demonstrated the steady production of *p*-coumaric acid and increasing level of (2*S*)-naringenin in the engineered strain Nar_{modABC} upon entry to stationary phase (Fig. 6e). As a result, the final (2*S*)-naringenin titer reached 4.6-fold (138.9 mg/L) higher than that of Nar_{modA} (30.2 mg/L) in shake flasks and the titer of *p*-coumaric acid stayed nearly constant at around 70 mg/L. Compared with the significant increment of *p*-coumaric acid in the stationary phase of strains contains Layer I or Layer I + II (Fig. 5c–f), these results showed that Layer III can effectively utilize *p*-coumaric acid to enhance the biosynthesis of (2*S*)-naringenin. However, a significantly reduced maximum OD_{600} of Nar_{modABC} was observed (Fig. 6e) suggesting that the combination of these three layers without expression optimization can inhibit cell growth. Thus, this prompted us to apply a directed evolution strategy to fine-tune the expression level for DRN to rapidly and accurately balance the multiple artificial metabolic systems, and achieve the highest (2*S*)-naringenin titer without impairing cell growth.

2.7. Directed evolution to fine-tune DRN and achieve high level production

To tune the constructed DRN via directed evolution, we established a fluorescent-activated cell sorting (FACS)-based high-throughput screening approach (Supplementary Fig. 3a). A TtgR-based (2*S*)-naringenin biosensor (Rogers et al., 2015) was constructed for investigating sorting parameters (Fig. 7a) leveraging the higher maximum detection limit of this sensor (~220 mg/L) comparing with other biosensors FdeR (10 mg/L; Fig. 3b) (Siedler et al., 2014; Wassem et al., 2017) and (2S)-naringenin riboswitch (<100 mg/L) (Jang et al., 2017; Xiu et al., 2017). To normalize across cell size and general expression issues, we utilized a constitutively expressing far-red fluorescent protein mKate2 (Rogers and Church, 2016) (Fig. 7a). As shown in Fig. 7b, the TtgR biosensor exhibited a linear correlation between (2*S*)-naringenin concentration and GFP fluorescence when (2*S*)-naringenin was lower than 220 mg/L with a maximum induction of 16.6-fold (GFP fluorescence declined when (2*S*)-naringenin was greater than 220 mg/L). Additionally, we observed a negative correlation between the FRFP fluorescence and (2*S*)-naringenin concentration likely due to the cell burden caused by high expression of GFP. As a result, we sought to identify cells that exhibit high green fluorescence and low red fluorescence as they are likely candidates for high performance.

To fine-tune the function and performance of our DRN system, the P_{fdeR}-P_{fdeA} of Layer II and P_{cspA} of Layer III were randomly mutated and then sorted through FACS (Fig. 7c). The mutant library sizes were 2.02×10^7 and 1.5×10^6 for Layer II and III, respectively. After fermentation, the high naringenin-producing strains were sorted and then screened

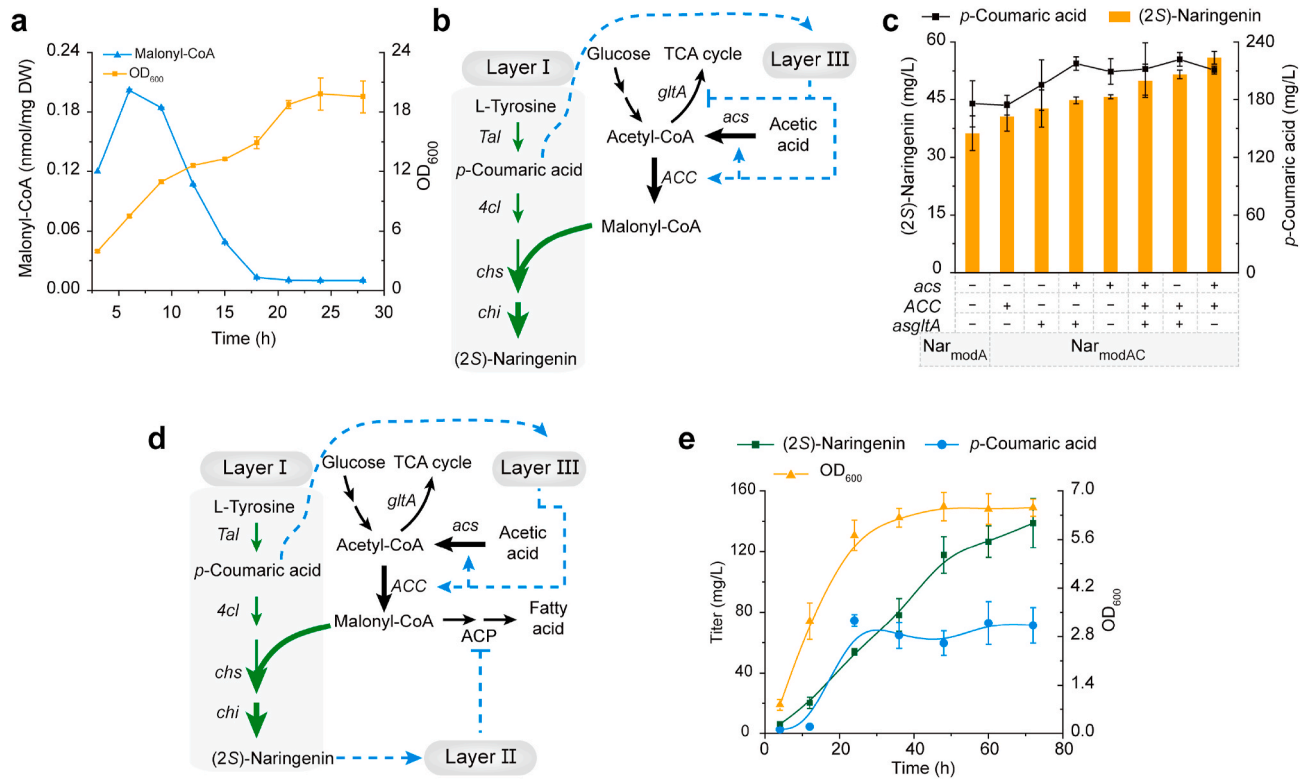

Fig. 6. The mechanisms and properties of *p*-coumaric acid-responsive dynamic regulation strains. **a**: The malonyl-CoA concentration in wild type *E. coli* BL21 at different growth stages. **b**: The regulation mechanisms of strain Nar_{modAC}. **c**: Optimization of Layer III through the combinatorial gene overexpression to generate various Nar_{modAC} constructs. Nar_{modA} was used as control. + or - represent the related genes were overexpressed or not, respectively. **d**: The regulation mechanisms of strain Nar_{modABC}. Layer II and III were pACM-FdeR-*acpH*-as*acpT*-as*acpS* and pRSM-PadR-*acs*-*ACC*, respectively. **e**: The (2*S*)-naringenin, *p*-coumaric acid, and OD_{600} level in Nar_{modABC} were determined. Means are reported, and the error bars represent standard deviation of biological triplicates.

using a 96-well deep well plate assays (Supplementary Fig. 3a-c) (Zhou et al., 2019). Among the variants tested, the best performing strain produced 251.4 mg/L (2*S*)-naringenin and 88.3 mg/L *p*-coumaric acid in the shake flask (Fig. 7d). Specifically, a 2.7-fold improvement in (2*S*)-naringenin production was achieved when compared with the base strain harboring an unoptimized layer I, II, and III. In order to characterize mutations in P_{fdeR}-P_{fdeA} and P_{cspA} of derived mutants, the promoter sequences and their relative expression strength were further analyzed (more details in Supplementary Fig. 4-6 and Supplementary Notes). Finally, we found that the excessively high level of *acpH* expression is negative to (2*S*)-naringenin production. This phenomenon is possibly due to a redundant cycle rendered by AcpH that burns 2 ATP per cycle for conversion of ACP_{active} into $ACP_{inactive}$ (Polacco and Cronan, 1981). While such a transition can effectively down-regulate fatty acid biosynthesis, it is quite costly to the cell and ultimately outweighs malonyl-CoA saving.

In order to further improve the titer, we used our previously established temperature-shift fermentation approach to produce (2*S*)-naringenin in an optimized medium (Zhou et al., 2020b). Comparing with the control strain (Nar_{modA}), Mut-17 exhibited 8.7-fold improvement in (2*S*)-naringenin production (523.7 ± 51.8 mg/L *v.s.* 59.8 ± 13.6 mg/L) and 11.4-fold reduction in the accumulation of *p*-coumaric acid (55.8 ± 22.2 mg/L *v.s.* 637.2 ± 9.6 mg/L) in the shake flasks (Fig. 7e–f). The significant titer improvement might be caused by the supplementation of extra malonyl-CoA generated by palmitic acid and stearic acid degradation. In order to verify the effects of NCOMB DRN, temperature-shift fermentation without the supplementation of fatty acids was performed. In this scenario, compared with Nar_{modA}, Mut-17 exhibited 7.3-fold improvement in (2*S*)-naringenin production (352.3 ± 45.5 mg/L *v.s.* 48.7 ± 3.7 mg/L) and 8.4-fold reduction in the accumulation of *p*-coumaric acid (85.8 ± 20.2 mg/L *v.s.* 717.2 ± 50.6 mg/L) in the shake flasks (Supplementary Fig. 7a and b). These results highlight the high-efficiency dynamic pathway regulation of the optimized NCOMB DRN. Moreover, we found that the expression of NCOMB DRN could increase the cell growth (OD_{600}) by 20% (8.5 ± 0.8 for Nar_{modA} *v.s.* 10.2 ± 0.6 for Mut-17), which probably caused by the lower accumulation level of *p*-coumaric acid that could repress cell growth (Fig. 7e–f) (Lou et al., 2012).

3. Discussion

Dynamic regulation of metabolic pathways marked with precise control of enzyme expression levels as well as optimal cell growth has received attention in the last few years (Dinh and Prather, 2019). In this study, we focus on optimizing and developing an NCOMB DRN to dynamically regulate the biosynthesis and conversion of malonyl-CoA at a single cell level to direct it toward (2*S*)-naringenin production. In our three-part scheme, the constitutively expressed (2*S*)-naringenin synthetic pathway (Layer I) is coupled with a (2*S*)-naringenin-responsive biosensor (Layer II) and a malonyl-CoA enhancer (Layer III) to establish a dynamic amplifier balancing cell growth and malonyl-CoA consumption (Fig. 1). It should be noted that in our approach, ACP uniquely serves as the regulatory target instead of the commonly used fatty acid synthase (Wu et al., 2014a). Like most synthetically designed circuits, it was necessary to optimize the interaction parameters in this system using FACS-based directed evolution. The underlying design and principles here have potential to be applied to produce other valuable target compounds if suitable biosensors are available.

Many advancements have been made in (2*S*)-naringenin production in recent years using static metabolic engineering strategies (Dunstan et al., 2020; Palmer et al., 2020; Pandey et al., 2016; Wu et al., 2014a, 2014b, 2015bib_Wu_et_al_2015bib_Wu_et_al_2014abib_Wu_et_al_2014b;

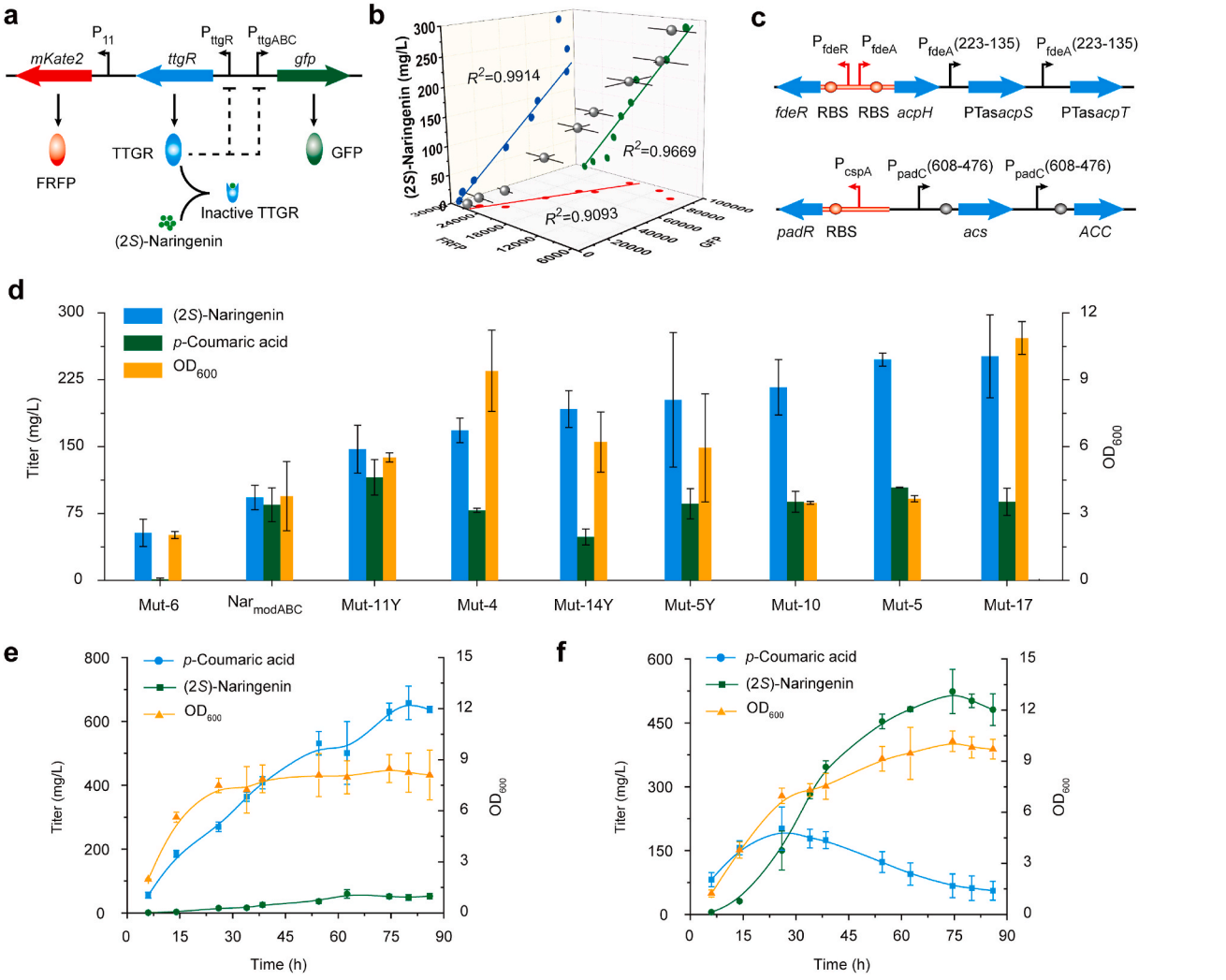

Fig. 7. The biosensor-based directed evolution and optimum strain fermentation. **a**: The structure of TtgR based (2*S*)-naringenin-responsive biosensor. **b**: The fluorescence levels of TtgR biosensor with different concentration of (2*S*)-naringenin inducer. **c**: The structure of Layer II and III. Red region represent the mutation area. **d**: The (2*S*)-naringenin, *p*-coumaric acid, and OD_{600} level in screened high producers. **e-f**: Comparison of fermentation profiles between the base strain Nar_{modA} (**e**) and the mutant Mut-17 (**f**). Means are reported, and the error bars represent standard deviation of biological triplicates.

Xu et al., 2011; Yang et al., 2015; Zhou et al., 2019). In order to balance the metabolic flux of (2*S*)-naringenin synthetic pathway, multi-modular regulation strategy (Wu et al., 2014b) and promoter library-based pathway optimization strategy (Gao et al., 2020; Zhou et al., 2019) were established to systemically optimize the expression level of TAL, 4CL, CHS, and CHI. Using such strategies, the titer of (2*S*)-naringenin reached up to 191.9 mg/L in *E. coli* when supplemented with L-tyrosine (Zhou et al., 2019). In this study, the (2*S*)-naringenin biosynthetic pathway was previously developed through a promoter library-based pathway optimization strategy (Zhou et al., 2019). However, the limited malonyl-CoA availability still restricted production. To address this issue, previous studies commonly selected fatty acid synthase as a repression target to reduce the consumption of malonyl-CoA. As a result, the malonyl-CoA concentration increased up to 4.5- and 8.8-fold when the *fabD* and *fabBF* were repressed by an asRNA system, respectively (Wu et al., 2014a; Yang et al., 2015). In comparison, repression of the activity of ACP in the present study exhibited a comparable result, which yielded a 7.5-fold improvement in malonyl-CoA production (Fig. 4). However, repression of fatty acid synthetic pathway significantly impaired the cellular growth (Wu et al., 2015; Xu et al., 2014; Zhou et al., 2020a). Hence, a dynamically regulated genetic circuit is essential for balancing the cell growth and production. In this work, the best (2*S*)-naringenin producer (Mut-17) leveraged both static metabolic engineering (Layer I) and dynamic metabolic engineering (Layer II and III), and finally achieved the balance between cell growth and production. Using Mut-17 as a chassis, we further optimized the fermentation conditions and the L-tyrosine synthetic pathway and achieved the titer of 588 mg/L (2*S*)-naringenin from glucose in 5-L bioreactor, the highest titer reported to date in *E. coli* (Zhou et al., 2020b). Among all nitrogen sources tested, media supplementation with NH_4Cl improved (2*S*)-naringenin production despite decreasing biomass formation compared to other rich components, such as peptone and yeast extract (Zhou et al., 2020b). Hence, it is necessary to optimize the fermentation strategies in bioreactors to simultaneously enhance cell growth and productivity in the future.

As a point of comparison with this work to other dynamic regulation strategies employed in the literature, it is well understood that intracellular malonyl-CoA content and impaired cell growth are the main challenges for (2*S*)-naringenin production (Wu et al., 2014a). To address these limitations, previous studies have implemented a QS system to enhance malonyl-CoA production after sufficient cell growth. For example, Christina et al. established a bifunctional quorum-sensing DRN, which can dynamically enhance the expression level of TAL as well as 4CL and retard malonyl-CoA consumption rate (Dinh and Prather, 2019). However, the reported (2*S*)-naringenin titer of best producer (125.9 mg/L) was only 24% of that of Mut-17 generated in this

study (523.7 ± 51.8 mg/L) (Fig. 7f). Comparison with NCOMB DRN used in this work, QS-based DRN suffered a signal distortion when transmission from cell density to gene expression. More specifically, we think the signal transition from cell density to malonyl-CoA concentration could not truly reflect the real demands for (2*S*)-naringenin production since cell growth state is also highly correlated to other factors including the energy and redox homeostasis (ATP/ADP and NADH/NAD^+), the supply of carbon and nitrogen sources, pH, and temperature (Shiloach and Fass, 2005). In this study, the established DRN could avoid such a distortion during signal transmission through directly sensing the accumulated (2*S*)-naringenin and *p*-coumaric acid to dynamically regulate gene expression, and finally achieve the goal of synchronizing cell growth and malonyl-CoA supplementation.

After comparing the intra- and extra-cellular metabolite levels, we confirmed that the intracellular concentration of (2*S*)-naringenin and *p*-coumaric acid in the engineered strain has much higher extracellular content, which ensured a low exchange rate of (2*S*)-naringenin and *p*-coumaric acid between individual single cells. In this background, we successfully demonstrate that the optimized NCOMB DRN allows dynamic regulation of the metabolic fluxes in single cells according to their cell profiles. After systemically optimizing the malonyl-CoA metabolic pathways, this strategy resulted in a 8.7-fold improvement in (2*S*)-naringenin production and 20% enhancement in cell growth, compared to the base strain. In terms of dynamic regulation at the spatiotemporal level, the spatial distribution properties of inducers directly influence the regulation mode of DRN at the single-cell level or population level. In this regard, it is possible to achieve the goal of switching regulatory modes between single-cell level and population level by a transporter engineering strategy which could alter the efficiency and direction of transmembrane transport to real-time re-allocate target molecules both intra- and extra-cellularly. On the other hand, we believe that rational design and optimize sophisticated DRNs via computational model (deep learning and machine learning models (Chen et al., 2019; Nielsen and Voigt, 2018)) can facilitate the improvement in the design accuracy and efficiency for more complex DRNs in the near future.

4. Materials and methods

4.1. Strains, medium, and culture conditions

E. coli JM109 and *E. coli* BL21 were used for plasmids construction and (2*S*)-naringenin production, respectively. LB medium was used to harvest cells for plasmid construction or fluorescence measurement. For the NCOMB DRN optimization process, (2*S*)-naringenin fermentation was performed at 30 °C with 220 rpm using MOPS minimal medium (supplemented with 10 g/L D-glucose, 1 g/L peptone, 3 mM L-tyrosine, and 4 g/L NH_4Cl). Temperature-shift fermentation was conducted as described in our previous report (Zhou et al., 2020b). In brief, the strain was cultured at 37 °C until OD_{600} reached 0.4 and then transferred to 25 °C in an optimized MOPS minimal medium containing 4 g/L NH_4Cl, 15 g/L glucose, 2.5 g/L glycerol, 7.5 g/L KAc, 2.5 g/L palmitic acid, 2.5 g/L stearic acid, and 5 g/L $CaCO_3$ at pH 7.0. Fermentation was performed at 250 mL shake flask scale. Streptomycin (100 μg/mL), ampicillin (100 μg/mL), chloramphenicol (34 μg/mL), and kanamycin (50 μg/mL) were added to the media when needed. The strains, plasmids, and primers used in this study are listed in Supplementary Table 1 and Table 2

4.2. Construction and characterization of biosensors

Restriction enzymes were purchased from Thermo Fisher Scientific (Waltham, MA). DNA ligase and PrimeSTAR HS DNA polymerase were purchased from Takara (Dalian, China). A ClonExpress II One Step Cloning Kit (Vazyme Biotech, Nanjing, China) or Gibson assembly method were used for plasmid construction. FdeR and P_{fdeA} promoter were synthesized and codon-optimized by Talen-bio Scientific (Shanghai) Co., Ltd.. Then, FdeR and P_{fdeA} promoter were amplified by primer pairs of FdeR(pACM)-F/FdeA-R, FdeR(pCOM)-F/FdeA-R, and FdeR(pRSM)-F/FdeA-R and cloned into *Apa*I/*Kpn*I, *Xba*I/*Kpn*I, and *Xba*I/*Kpn*I sites of pACM4, pCOM4, and pRSM3 to construct pACM-FdeR, pCOM-FdeR, and pRSM-FdeR, respectively. *gfp* was amplified by primer pairs of GFP-F/GFP-R and cloned into the *Spe*I/*Sal*I sites of plasmid pCDM4 to construct pCDM-GFP. Primer pairs of PfdeA(M)-F/PfdeA(N)-RBS-R or PfdeA(M)-F/PfdeA(1)-R were used to amplify different length of P_{fdeA} (M-N) promoters. Here, M and N represent the positions of amplified promoters, and the last 3′ base was defined as position 1. The amplified promoters were cloned into *Kpn*I/*Spe*I sites of pCDM-GFP to construct plasmids of pCDM-PfdeA(M-N)-GFP, *i.e.*, pCDM-PfdeA(180-1)-GFP, pCDM-PfdeA(223-1)-GFP, pCDM-PfdeA(250-1)-GFP, pCDM-PfdeA(288-1)-GFP, pCDM-PfdeA(220-50)-GFP, pCDM-PfdeA(220-83)-GFP, pCDM-PfdeA(220-135)-GFP, and pCDM-PfdeA(220-180)-GFP (Supplementary Fig. 1a). To characterize P_{fdeA} (M-N) promoters, the constructed pCDM-PfdeA(M-N)-GFP plasmids were transformed into control strain harboring a pRSM-FdeR plasmid (Supplementary Fig. 1a).

PadR and its terminator were amplified from the genome of *Bacillus subtilis* 168 by primer pairs of PadR-F/PadR-T-R. pRSM3 was digested by *Xba*I/*Kpn*I to obtain the 1.9 kb and 3.7 kb fragments which were subsequently ligated with PadR-terminator to construct plasmids of pRSM-PadR and pRSM-T_7-PadR, respectively. An exponential phase expressed promoter P_{cspA} was amplified from the genome of *E. coli* MG1655 by primer pairs of cspA-F/cspA-R. Then, P_{cspA} was cloned into *Xba*I/*Asc*I site of pRSM-PadR to construct plasmid pRSM-P_{cspA}-PadR. To simplify the structure of promoter P_{padC}, primer pairs of PadC-P-F/PadC-Q-R were used to amplify different lengths of P_{padC} from the genome of *Bacillus subtilis* 168. Here, P and Q represent the positions of amplified promoters, and the last 3′-base was defined as position 1. The amplified promoters P_{padC} (P-Q) were ligated with *gfp* by fusion PCR, and then such promoters were cloned into *Bam*HI/*Spe*I sites of pRSM-T7-PadR to construct the plasmids of pRSM-T7-PadR-P_{padC}(P-Q)-GFP (P-Q: 608-1, 608-496, 608-476, 608-456, 216-1, 216-39, 216-79, and 216-123). Furthermore, the P_{padC}-(608-476)-*gfp* fragment was cloned into *Bam*HI/*Spe*I sites of pRSM-P_{cspA}-PadR to construct the plasmids of pRSM-P_{cspA}-PadR-P_{padC}-(608-476)-GFP (Supplementary Fig. 1c).

To characterize the biosensors, strains were cultured in LB medium at 30 °C. Various concentrations of (2*S*)-naringenin, IPTG, or/and *p*-coumaric acid were added to induce the expression of GFP when the OD_{600} reached 0.4–0.6. After 8 h induction at 30 °C, cells were washed twice in PBS buffer (pH 7.4) and then fluorescence (488 nm excitation, 520 nm emission) and OD_{600} were measured by Cytation 3 imaging reader.

4.3. Pathway construction

Plasmid pUC57-asgltA that carried an anti-sense RNA gene of gltA (as*gltA*) was synthesized by Talen-bio Scientific (Shanghai) Co., Ltd.. Promoter P_{fdeA} (223-135) was amplified and cloned into *Not*I site of pUC57-asgltA to construct a pUC57-P_{fdeA}-asgltA plasmid. Furthermore, complementary sequences of mRNA of *acpT*, *acpS*, *acpP*, and *fabD* were amplified from *E. coli* genome by primer pairs of asacpT-F/asacpT-R, asacpS-F/asacpS-R, asacpP-F/asacpP-R, and asfabD-F/asfabD-R, and subsequently cloned into *Nco*I/*Xho*I sites of pUC57-P_{fdeA}-asgltA to construct plasmids of pUC57-P_{fdeA}-asacpT, pUC57-P_{fdeA}-asacpS, pUC57-P_{fdeA}-asacpP, and pUC57-P_{fdeA}-asfabD, respectively. Then, DNA fragments of P_{fdeA}-asacpT, P_{fdeA}-asacpS, P_{fdeA}-asacpP, and P_{fdeA}-asfabD were amplified from these plasmids by primer pairs of asRNA-F/asRNA-R. The *acpH* gene was amplified from the genome of *E. coli* MG1655 by primer pairs of acpH-F/acpH-R, and subsequently cloned into *Kpn*I/*Spe*I sites of pACM-FdeR, pCOM-FdeR, and pRSM-FdeR to construct plasmids of pACM-FdeR-acpH, pCOM-FdeR-acpH, and pRSM-FdeR-acpH, respectively. Finally, P_{fdeA}-asacpT, P_{fdeA}-asacpS, P_{fdeA}-asacpP, and P_{fdeA}-asfabD were digested by *Avr*II/*Sal*I, and subsequently cloned into

*Nhe*I/*Sal*I sites of pACM-FdeR-acpH, pCOM-FdeR-acpH, and pRSM-FdeR-acpH by ePathBrick approach (Xu et al., 2012) to construct Layer II plasmids of pACM-FdeR-*acpH*-as*acpT*, pCOM-FdeR-*acpH*-as*acpT*, pRSM-FdeR-*acpH*-as*acpT*, pACM-FdeR-*acpH*-as*acpT*-as*acpS*, pCOM-FdeR-*acpH*-as*acpT*-as*acpS*, pRSM-FdeR-*acpH*-as*acpT*-as*acpS*, pACM-FdeR-*acpH*-as*acpT*-as*acpS*-as*acpP*, pACM-FdeR-*acpH*-as*acpT*-as*acpS*-as*fabD*, and pACM-FdeR-*acpH*-as*acpT*-as*acpS*-as*acpP*-as*fabD*. *E. coli* strains that harbor these plasmids were cultured and induced by 100 mg/L (2*S*)-naringenin when OD_{600} reached 0.2. After 2 h induction, cells were harvested to measure the intracellular concentration of CoA and its esters.

Promoter P_{padC} (608-476) was amplified by primer pairs of padC-ACC-F/padC-476-ACC-R and padC-*Spe*I-F/padC476-acs-R, and subsequently ligated with ACC and *acs* to construct DNA fragments of P_{padC}(608-476)-ACC and P_{padC}(608-476)-acs, respectively. The ACC genes (*accBC* and *dtsR1*) and *acs* were obtained from our previous study (Zhu et al., 2014). Promoter P_{padC} (608-496) was amplified by primer pairs of padC-*Spe*I-F/padC496-as*gltA*-R, and subsequently ligated with as*gltA* to construct DNA fragments of P_{padC}(608-496)-asgltA. DNA fragments of P_{padC}(608-496)-asgltA and P_{padC}(608-476)-acs were cloned into *Xba*I/*Nde*I sites of pRSM-P_{cspA}-PadR by ePathBrick approach (Xu et al., 2012) to construct plasmids of pRSM-PadR-acs, pRSM-PadR-asgltA, and pRSM-PadR-acs-asgltA. Then, P_{padC}(608-476)-ACC was cloned into *Bam*HI/*Spe*I sites of pRSM-P_{cspA}-PadR, pRSM-PadR-acs, pRSM-PadR-asgltA, pRSM-PadR-acs-asgltA to construct plasmids of pRSM-PadR-ACC, pRSM-PadR-acs-ACC, pRSM-PadR-asgltA-ACC, and pRSM-PadR-acs-asgltA-ACC, respectively.

4.4. FACS-based directed evolution

Far-red fluorescent protein (mKate2) and constitutive promoter P_{11} were amplified from plasmid pJKR-H-benM (Rogers and Church, 2016) with the primer pair of FRFP-F/FRFP-R. (2*S*)-Naringenin-responsive biosensor (including TtgR, GFP, and promoter P_{ttgR} and P_{ttgABC}) was amplified from pJKR-H-ttgR (Rogers et al., 2015) with the primer pair of TtgR-F/GFP-R. Then the PCR products of mKate2 and (2*S*)-naringenin biosensor were cloned into *Xba*I/*Bam*HI sites of pCDM-P_{ssrA}-UTR_{rpsT}-CHS-$PUTR_{glpD}$-CHI by Gibson assembly method to construct the final plasmid pCDM-CHS-CHI-TtgR-GFP-FRFP.

GeneMorph II Random Mutagenesis Kit was used to generate mutation libraries of $P_{fdeR\text{-}mut}$-$P_{fdeA\text{-}mut}$ and $P_{cspA\text{-}mut}$ with high mutation rate. Then the libraries were Gibson assembled with linearized plasmids of pACM-FdeR-acpH-asacpT-asacpS and RSM-PadR-acs-ACC to construct plasmid libraries of pACM-$P_{fdeR\text{-}mut}$-FdeR-$P_{fdeA\text{-}mut}$-acpH-asacpT-asacpS and pRSM-$P_{cspA\text{-}mut}$-PadR-acs-ACC, respectively. Finally, these libraries were transformed into a *E. coli* strain which carried a constitutively expressing (2S)-naringenin synthetic pathway (Layer I) to generate a dynamic regulation library of *E. coli* Nar_{lib}.

To perform the flow cytometry sorting, *E. coli* Nar_{lib} was cultured at 30 °C and 220 rpm in MOPS medium for 24 h. Then cells were diluted to OD_{600} of 0.5. BD FACSAria III equipped with a 70 μm nozzle, 561 nm and 488 nm laser for excitation, and 610/20 nm and 530/30 nm filter was used for the sorting. The top 0.1% of single cells with high green fluorescence and low red fluorescence were sorted out from the mutant library (approximately 5×10^4). The sorted cells were cultured in LB medium for 8 h at 37 °C and then spread on agar plates. Approximately 3000 single colonies were picked into 96-deep-well plates containing 1 mL of MOPS medium in each well to screen high-titer strains by following our previously reported high-throughput screening method (Zhou et al., 2019). The high producers were further selected and fermented in 250 mL shaking flasks with biological triplicate. Finally, the mutation region of the selected high-titer strains was sequenced.

4.5. Real-time fluorescence quantitative PCR

Strains were cultured in MOPS medium at 30 °C with 220 rpm orbital shaking. Cells were then harvested at 4 °C with centrifuge speed 3000×*g* for 3 min mRNA was extracted from the harvested cells according to the manufacturer's instructions of a RNAprep Pure Cell/Bacteria Kit (Tiangen, Beijing, China). PrimeScript RT reagent Kit with gDNA Eraser (TaKaRa, Japan) was used to reverse transcribe the extracted mRNA. SYBR Premix Ex Taq (Tli RNaseH Plus) was used for qRT-PCR on a LightCycler 480 II thermal cycler system (Roche, Mannheim, Germany). 16S rRNA gene was selected as internal standard.

4.6. Chromatography analysis methods

Equivalent volume of fermentation samples was mixed with ethanol at room temperature to extract total (2*S*)-naringenin and *p*-coumaric acid. Then the mixtures were ultrasonicated for 3 min and left at room temperature for 30 min to completely extract products. The supernatant was collected after centrifugation (4 °C, 10000×*g*, 5 min) and filtered through 0.22 μm hydrophobic membranes. These supernatants were analyzed using an Agilent 1260 HPLC system. (2*S*)-Naringenin and *p*-coumaric acid were separated by a reverse-phase Gemini NX-C18 column (4.6 × 250 mm) at 25 °C. Gradient elution method was the same as described in our previous report (Zhou et al., 2019).

In order to measure the concentration of CoA and its thioester, strains were cultured until OD_{600} reached 0.2, and then cells were harvested after induction by 100 mg/L of (2S)-naringenin for 2 h. CoA, acetyl-CoA, and malonyl-CoA were extracted according to the previously described method (Zha et al., 2009). Shim-pack VP-ODS (250 L × 2.0) UPLC column (Shimadzu, Tokyo, Japan) was used to separate CoA and its thioesters at 40 °C with 15 mM ammonium formate in water (A) and 10 mM ammonium acetate in methanol (B) as mobile phases. The elution procedure was used as following: 0.2 mL/min flow rate, 10–25% B (vol/vol) for 5 min, 25–100% B (vol/vol) for 10 min, 100-10% B (vol/vol) for 1 min, maintaining 10% B (vol/vol) for 2 min. For quantitative analysis of CoA and its thioesters, the extracted ion chromatogram (EIC) peak areas were calculated by Shimadu LCMS-IT-TOF (Shimadzu, Kyoto, Japan). The detected EICs were: $[M\text{-}H]^-$ = 766.5299 *m/z* for CoA, $[M+H]^+$ = 810.5813 m/z for acetyl-CoA, $[M\text{-}H]^-$ = 852.5764 *m/z* for malonyl-CoA. All the experiments were performed with biological triplicate. Means are reported, and the error bars represent standard deviation of biological triplicate experiments.

4.7. Intracellular and extracellular products measurement

According to the previous reports, the *E. coli* volume was evaluated as 0.65 ± 0.5 μm^3 (Allen et al., 2014; Kubitschek, 1990). Cell numbers were counted by a 16 × 25 blood cell counting plate under a microscope. Firstly, 10 mL of fermentation samples were centrifuged at 4 °C, 3000×*g* for 5 min to obtain cells and supernatant. The supernatant was directly used to measure the extracellular concentration of (2*S*)-naringenin and *p*-coumaric acid. The pelleted cells were subsequently resuspended in 300 μl of ethanol, ultrasonicated for 3 min, and left at room temperature for 30 min. Then the resulting cell debris was removed and the supernatant was used to measure the intracellular level of (2*S*)-naringenin and *p*-coumaric acid. The intracellular concentration of (2*S*)-naringenin and *p*-coumaric acid was calculated as equation (1).

$$Ci = \frac{a \times Cd}{Vc \times Dc \times Vs} \quad (1)$$

Ci ~ Intracellular concentration of (2*S*)-naringenin and *p*-coumaric acid;
Cd ~ The detected concentration of (2*S*)-naringenin and *p*-coumaric acid that were extracted from cells;
a 300 μl of ethanol;
Vc ~ *E. coli* cell volume;
Dc ~ Cell density;
Vs~ 10 mL of sample volume.

4.8. Nucleic acid sequences

The nucleic acid sequences of genes, promoters, and anti-sense RNAs were listed in Supplementary Table 3 of Supplementary materials.

CRediT authorship contribution statement

Shenghu Zhou: Conceptualization, Methodology, Investigation, Visualization, Writing – original draft. **Shuo-Fu Yuan:** Investigation, Formal analysis, Validation, Writing – original draft. **Priya H. Nair:** Investigation. **Hal S. Alper:** Conceptualization, Resources, Writing – review & editing. **Yu Deng:** Conceptualization, Supervision, Resources, Writing – review & editing. **Jingwen Zhou:** Conceptualization, Supervision, Resources, Funding acquisition, Writing – review & editing.

Declaration of competing interest

The authors declare no competing interests.

Acknowledgements

This work was supported by the National Key Research and Development Program of China (2019YFA0904800), the National Science Fund for Excellent Young Scholars (21822806), the National Natural Science Foundation of China (31900066, 21877053, 31770097), the Air Force Office of Scientific Research under Award No. FA9550-14-1-0089, the National First-class Discipline Program of Light Industry Technology and Engineering (LITE2018-24), the Fundamental Research Funds for the Central Universities (JUSRP12056, JUSRP51705A).

Appendix A. Supplementary data

Supplementary data to this article can be found online at https://doi.org/10.1016/j.ymben.2021.05.007.

Author contributions

S.Z., J.Z., and Y.D. conceived the idea. S.Z. performed the experiments and data analysis. S.Z. and S.-F.Y. did the directed evolution. S.-F.Y. and P.H.N. did the 96-well plate screening. H.S.A. suggested the design idea of *p*-coumaric acid biosensor and supported the directed evolution. H.S.A., Y.D., and J.Z. critically reviewed the manuscript. S.Z., and S.-F.Y. wrote the paper. All authors reviewed, approved and contributed to the final version of the manuscript.

References

Allen, C., Loo, J.F., Yu, S., Kong, S., Chan, T.-F., 2014. Monitoring bacterial growth using tunable resistive pulse sensing with a pore-based technique. Appl. Microbiol. Biotechnol. 98, 855–862.

Bretschneider, T., Zocher, G., Unger, M., Scherlach, K., Stehle, T., Hertweck, C., 2011. A ketosynthase homolog uses malonyl units to form esters in cervimycin biosynthesis. Nat. Chem. Biol. 8, 154.

Chan, D.I., Vogel, H.J., 2010. Current understanding of fatty acid biosynthesis and the acyl carrier protein. Biochem. J. 430, 1–19.

Chen, K.M., Cofer, E.M., Zhou, J., Troyanskaya, O.G., 2019. Selene: a PyTorch-based deep learning library for sequence data. Nat. Methods 16, 315–318.

David, F., Nielsen, J., Siewers, V., 2016. Flux control at the malonyl-CoA node through hierarchical dynamic pathway regulation in *Saccharomyces cerevisiae*. ACS Synth. Biol. 5, 224–233.

Dinh, C.V., Prather, K.L., 2019. Development of an autonomous and bifunctional quorum-sensing circuit for metabolic flux control in engineered *Escherichia coli*. Proc. Natl. Acad. Sci. U.S.A. 116, 25562-25568.

Dunstan, M.S., Robinson, C.J., Jervis, A.J., Yan, C., Carbonell, P., Hollywood, K.A., Currin, A., Swainston, N., Le Feuvre, R., Micklefield, J., Faulon, J.-L., Breitling, R., Turner, N., Takano, E., Scrutton, N.S., 2020. Engineering Escherichia coli towards de novo production of gatekeeper (2*S*)-flavanones: naringenin, pinocembrin, eriodictyol and homoeriodictyol. Synthetic Biology (in press).

Gao, S., Zhou, H., Zhou, J., Chen, J., 2020. Promoter library based pathway optimization for efficient (2*S*)-naringenin production from *p*-coumaric acid in *Saccharomyces cerevisiae*. J. Agric. Food Chem. 68, 6884–6891.

Ge, C., Sheng, H.K., Chen, X., Shen, X.L., Sun, X.X., Yan, Y.J., Wang, J., Yuan, Q.P., 2020. Quorum sensing system used as a tool in metabolic engineering. Biotechnol. J. 15 e1900360.

Heil, C.S., Wehrheim, S.S., Paithankar, K.S., Grininger, M., 2019. Fatty acid biosynthesis: chain-length regulation and control. Chembiochem 20, 2298–2321.

Jang, S., Jang, S., Xiu, Y., Kang, T.J., Lee, S.-H., Koffas, M.A., Jung, G.Y., 2017. Development of artificial riboswitches for monitoring of naringenin in vivo. ACS Synth. Biol. 6, 2077–2085.

Kubitschek, H., 1990. Cell volume increase in Escherichia coli after shifts to richer media. J. Bacteriol. 172, 94–101.

Lou, Z., Wang, H., Rao, S., Sun, J., Ma, C., Li, J., 2012. p-Coumaric acid kills bacteria through dual damage mechanisms. Food Contr. 25, 550–554.

Milke, L., Marienhagen, J., Engineering intracellular malonyl-CoA availability in microbial hosts and its impact on polyketide and fatty acid synthesis. Appl. Microbiol. Biotechnol.. 104, 6057-6065.

Minagawa, S., Inami, H., Kato, T., Sawada, S., Yasuki, T., Miyairi, S., Horikawa, M., Okuda, J., Gotoh, N., 2012. RND type efflux pump system MexAB-OprM of pseudomonas aeruginosa selects bacterial languages, 3-oxo-acyl-homoserine lactones, for cell-to-cell communication. BMC Microbiol. 12, 70.

Moser, F., Borujeni, A.E., Ghodasara, A.N., Cameron, E., Park, Y., Voigt, C.A., 2018. Dynamic control of endogenous metabolism with combinatorial logic circuits. Mol. Syst. Biol. 14 e8605.

Nguyen, T.K.C., Tran, N.P., Cavin, J.-F., 2011. Genetic and biochemical analysis of PadR–*padC* promoter interactions during the phenolic acid stress response (PASR) in *Bacillus subtilis* 168. J. Bacteriol. 196, 4180–4191.

Nielsen, A.A., Voigt, C.A., 2018. Deep learning to predict the lab-of-origin of engineered DNA. Nat. Commun. 9, 1–10.

Palmer, C.M., Miller, K.K., Nguyen, A., Alper, H.S., 2020. Engineering 4-coumaroyl-CoA derived polyketide production in *Yarrowia lipolytica* through a β-oxidation mediated strategy. Metab. Eng. 57, 174–181.

Pandey, R.P., Parajuli, P., Koffas, M.A.G., Sohng, J.K., 2016. Microbial production of natural and non-natural flavonoids: pathway engineering, directed evolution and systems/synthetic biology. Biotechnol. Adv. 34, 634–662.

Pearson, J.P., Van Delden, C., Iglewski, B.H., 1999. Active efflux and diffusion are involved in transport of *Pseudomonas aeruginosa* cell-to-cell signals. J. Bacteriol. 181, 1203–1210.

Polacco, M.L., Cronan, J.E., 1981. A mutant of Escherichia coli conditionally defective in the synthesis of holo-[acyl carrier protein]. J. Biol. Chem. 256, 5750–5754.

Ran, F.A., Hsu, Patrick D., Lin, C.-Y., Gootenberg, Jonathan S., Konermann, S., Trevino, A.E., Scott, David A., Inoue, A., Matoba, S., Zhang, Y., Zhang, F., 2013. Double nicking by RNA-guided CRISPR Cas9 for enhanced genome editing specificity. Cell 154, 1380–1389.

Reese, M.G., 2001. Application of a time-delay neural network to promoter annotation in the *Drosophila melanogaster* genome. Comput. Chem. 26, 51–56.

Rogers, J.K., Church, G.M., 2016. Genetically encoded sensors enable real-time observation of metabolite production. Proc. Natl. Acad. Sci. U.S.A. 113, 2388–2393.

Rogers, J.K., Guzman, C.D., Taylor, N.D., Raman, S., Anderson, K., Church, G.M., 2015. Synthetic biosensors for precise gene control and real-time monitoring of metabolites. Nucleic Acids Res. 43, 7648–7660.

Schmidt, F.R., 2005. Optimization and scale up of industrial fermentation processes. Appl. Microbiol. Biotechnol. 68, 425–435.

Shen, X.L., Wang, J., Li, C.Y., Yuan, Q.P., Yan, Y.J., 2019. Dynamic gene expression engineering as a tool in pathway engineering. Curr. Opin. Biotechnol. 59, 122–129.

Shiloach, J., Fass, R., 2005. Growing *E. coli* to high cell density—a historical perspective on method development. Biotechnol. Adv. 23, 345–357.

Sibon, O.C., Strauss, E., 2016. Coenzyme A: to make it or uptake it? Nat. Rev. Mol. Cell Biol. 17, 605–606.

Siedler, S., Khatri, N.K., Zsohár, A., Kjærbølling, I., Vogt, M., Hammar, P., Nielsen, C.F., Marienhagen, J., Sommer, M.O.A., Joensson, H.N., 2017. Development of a bacterial biosensor for rapid screening of yeast *p*-coumaric acid production. ACS Synth. Biol. 6, 1860–1869.

Siedler, S., Stahlhut, S.G., Malla, S., Maury, J., Neves, A.R., 2014. Novel biosensors based on flavonoid-responsive transcriptional regulators introduced into *Escherichia coli*. Metab. Eng. 21, 2–8.

Singh, V., Haque, S., Niwas, R., Srivastava, A., Pasupuleti, M., Tripathi, C.K.M., 2017. Strategies for fermentation medium optimization: an in-depth review. Front. Microbiol. 7.

Takamura, Y., Nomura, G., 1988. Changes in the intracellular concentration of acetyl-CoA and malonyl-CoA in relation to the carbon and energy metabolism of *Escherichia coli* K12. J. Gen. Microbiol. 134, 2249–2253.

Thomas, J., Cronan, J.E., 2005. The enigmatic acyl carrier protein phosphodiesterase of *Escherichia coli*: genetic and enzymological characterization. J. Biol. Chem. 280, 34675-34683.

Tian, J., Yang, G., Gu, Y., Sun, X., Lu, Y., Jiang, W., 2020. Developing an endogenous quorum-sensing based CRISPRi circuit for autonomous and tunable dynamic regulation of multiple targets in Streptomyces. Nucleic Acids Res. 48, 8188–8202.

Tran, N.P., Gury, J., Dartois, V., Nguyen, T.K.C., Seraut, H., Barthelmebs, L., Gervais, P., Cavin, J.-F., 2008. Phenolic acid-mediated regulation of the *padC* gene, encoding the phenolic acid decarboxylase of *Bacillus subtilis*. J. Bacteriol. 190, 3213–3224.

Wassem, R., Marin, A.M., Daddaoua, A., Monteiro, R.A., Chubatsu, L.S., Ramos, J.L., Deakin, W.J., Broughton, W.J., Pedrosa, F.O., Souza, E.M., 2017. A NodD-like protein activates transcription of genes involved with naringenin degradation in a flavonoid-dependent manner in *Herbaspirillum seropedicae*. Environ. Microbiol. 19, 1030–1040.

Wu, J.J., Du, G.C., Chen, J., Zhou, J.W., 2015. Enhancing flavonoid production by systematically tuning the central metabolic pathways based on a CRISPR interference system in *Escherichia coli*. Sci Rep-UK 5, 13477.
Wu, J.J., Du, G.C., Zhou, J.W., Chen, J., 2013. Metabolic engineering of *Escherichia coli* for (2*S*)-pinocembrin production from glucose by a modular metabolic strategy. Metab. Eng. 16, 48–55.
Wu, J.J., Yu, O., Du, G.C., Zhou, J.W., Chen, J., 2014a. Fine-tuning of the fatty acid pathway by synthetic antisense RNA for enhanced (2*S*)-naringenin production from L-tyrosine in *Escherichia coli*. Appl. Environ. Microbiol. 80, 7283–7292.
Wu, J.J., Zhou, T.T., Du, G.C., Zhou, J.W., Chen, J., 2014b. Modular optimization of heterologous pathways for de novo synthesis of (2*S*)-naringenin in *Escherichia coli*. PloS One 9 e101492.
Xiao, Y., Bowen, C.H., Liu, D., Zhang, F., 2016. Exploiting nongenetic cell-to-cell variation for enhanced biosynthesis. Nat. Chem. Biol. 12, 339.
Xiu, Y., Jang, S., Jones, J.A., Zill, N.A., Linhardt, R.J., Yuan, Q., Jung, G.Y., Koffas, M.A. G., 2017. Naringenin-responsive riboswitch-based fluorescent biosensor module for *Escherichia coli* co-cultures. Biotechnol. Bioeng. 114, 2235–2244.
Xu, J.-Y., Xu, Y., Chu, X., Tan, M., Ye, B.-C., 2018. Protein acylation affects the artificial biosynthetic pathway for pinosylvin production in engineered *E. coli*. ACS Chem. Biol. 13, 1200–1208.
Xu, P., Li, L.Y., Zhang, F.M., Stephanopoulos, G., Koffas, M., 2014. Improving fatty acids production by engineering dynamic pathway regulation and metabolic control. Proc. Natl. Acad. Sci. U.S.A. 111, 11299-11304.
Xu, P., Ranganathan, S., Fowler, Z.L., Maranas, C.D., Koffas, M.A., 2011. Genome-scale metabolic network modeling results in minimal interventions that cooperatively force carbon flux towards malonyl-CoA. Metab. Eng. 13, 578–587.
Xu, P., Vansiri, A., Bhan, N., Koffas, M.A.G., 2012. ePathBrick: a synthetic biology platform for engineering metabolic pathways in *E. coli*. ACS Synth. Biol. 1, 256–266.
Yang, Y., Lin, Y., Li, L., Linhardt, R.J., Yan, Y., 2015. Regulating malonyl-CoA metabolism via synthetic antisense RNAs for enhanced biosynthesis of natural products. Metab. Eng. 29, 217–226.
Zha, W.J., Rubin-Pitel, S.B., Shao, Z.Y., Zhao, H.M., 2009. Improving cellular malonyl-CoA level in Escherichia coli via metabolic engineering. Metab. Eng. 11, 192–198.
Zhang, B., Zhou, N., Liu, Y.M., Liu, C., Lou, C.B., Jiang, C.Y., Liu, S.J., 2015. Ribosome binding site libraries and pathway modules for shikimic acid synthesis with *Corynebacterium glutamicum*. Microb. Cell Factories 14, 71.
Zhao, E.M., Suek, N., Wilson, M.Z., Dine, E., Pannucci, N.L., Gitai, Z., Avalos, J.L., Toettcher, J.E., 2019. Light-based control of metabolic flux through assembly of synthetic organelles. Nat. Chem. Biol. 15, 589–597.
Zheng, Y., Meng, F., Zhu, Z., Wei, W., Sun, Z., Chen, J., Yu, B., Lou, C., Chen, G.-Q., 2019. A tight cold-inducible switch built by coupling thermosensitive transcriptional and proteolytic regulatory parts. Nucleic Acids Res. 47 e137.
Zhou, S., Ding, R., Chen, J., Du, G., Li, H.Z., Zhou, J., 2017. Obtaining a panel of cascade promoter-5'-UTR complexes in *Escherichia coli*. ACS Synth. Biol. 6, 1065–1075.
Zhou, S., Hao, T., Xu, S., Deng, Y., 2020a. Coenzyme A thioester-mediated carbon chain elongation as a paintbrush to draw colorful chemical compounds. Biotechnol. Adv. 43, 107575.
Zhou, S., Hao, T., Zhou, J., 2020b. Fermentation and metabolic pathway optimization to de novo synthesize (2S)-naringenin in Escherichia coli. J. Microb. Biotechnol. 30, 1575–1583.
Zhou, S., Lyu, Y., Li, H., Koffas, M.A., Zhou, J., 2019. Fine-tuning the (2S)-naringenin synthetic pathway using an iterative high-throughput balancing strategy. Biotechnol. Bioeng. 116, 1392–1404.
Zhu, S.J., Wu, J.J., Du, G.C., Zhou, J.W., Chen, J., 2014. Efficient synthesis of eriodictyol from L-tyrosine in *Escherichia coli*. Appl. Environ. Microbiol. 80, 3072–3080.